Nanoscale

Accepted Manuscript

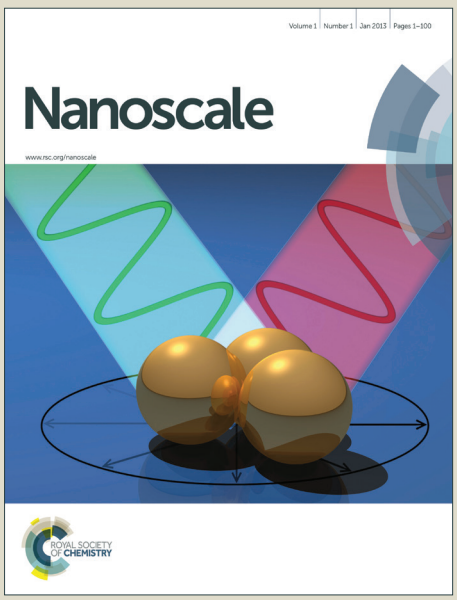

ROYAL SOCIETY OF CHEMISTRY

www.rsc.org/nanoscale

Cite this: DOI: 10.1039/c0xx00000x

www.rsc.org/xxxxxx

ARTICLE TYPE

Porous Ni-Mn oxide nanosheets *in-situ* formed on nickel foam as 3D hierarchical monolith de-NO_x catalysts

Sixiang Cai, Dengsong Zhang*, Liyi Shi, Jing Xu, Lei Zhang, Lei Huang, Hongrui Li and Jianping Zhang

Received (in XXX, XXX) Xth XXXXXXXXX 20XX, Accepted Xth XXXXXXXXX 20XX

DOI: 10.1039/b000000x

Abstract: In this work, we successfully *in-situ* decorated the nickel foam with porous Ni-Mn oxide nanosheets (3DH-NM/NF) as 3D hierarchical monolith de-NO_x catalysts *via* a simple hydrothermal reaction and calcination process. The catalysts were carefully examined by X-ray diffraction, scanning electron microscopy, transmission electron microscopy, elemental mapping, X-ray photoelectron spectroscopy, H_2 temperature-programmed reduction and NH_3 temperature-programmed desorption measurements. The results indicated that the nanosheets are composed of $Ni_6Mn_1O_8$ spinel and the metal species are uniformly dispersed in the bi-metal oxides. As a result, the strong synergistic effects between the Mn and Ni species have been observed. The active oxygen species, reducible species and acidity are enhanced by the *in-situ* formation of the nanosheets on the surface of nickel foam. These desirable features of 3DH-NM/NF catalysts bring about the excellent de-NO_x performance. Moreover, the 3DH-NM/NF catalysts also present good stability and H_2O resistance. Based on these favorable properties, the 3DH-NM/NF could be considered as a promising candidate for the monolith de-NO_x catalysts.

1. Introduction

Nitrogen oxides (NO_x) emitted from coal and fossil fuel combustion can cause great environmental problems including acid rain, photo chemical smog and greenhouse effect. [1-4] Up to date, the selective catalytic reduction of NO by ammonia (NH_3-SCR) has been considered as the most effective and economical technology for the removal of NO_x from the mobile or stationary sources.[5-7] For decades, V_2O_5-MoO_3/TiO_2 and V_2O_5-WO_3/TiO_2 were used in many countries as industrially adopted NH_3-SCR catalysts.[8-10] Nevertheless, this class of catalysts suffers from some drawbacks such as relatively high operation temperature, the low N_2 selectivity as well as the toxicity to the environment and human health. Therefore, extensive efforts should be devoted to develop non-vanadium catalysts for the NH_3-SCR application.

Recently, many research efforts have been made to the manganese based catalysts due to the inherently environmentally benign character and the outstanding catalytic performance in the NH_3-SCR of NO.[11-18] In recent literatures, Wan *et al.* discovered the strong interaction between the Mn and Ni species in the Ni-Mn bi-metal oxides, leading to great catalytic activities of NO_x removal.[19] Boningari *et al.* investigated the Mn/TiO_2 and the Ni-Mn/TiO_2 catalysts and found the improved de-NO_x performance by the introduction of Ni species.[12] It has been demonstrated that the Ni-Mn bi-metal oxides could act as a promising candidate for NH_3-SCR of NO. However, for practical application, the active components were usually immobilized on the surface or mixed into the channel walls of ceramic monoliths or parallel passage reactors by wash coating, dip coating, impregnation or extrusion.[10, 20-22] In the actual operation process, the random distribution of active components, the low inter-phase mass transfer ability and the blockage of channel could lead to the decreasing of catalytic activity.[23] Therefore, it is still a challenge to develop new synthetic strategies and catalyst support in order to fabricate novel Ni-Mn monolith catalysts with high de-NO_x activity, mass transfer ability and stability.

Owing to the high porosity, stability, thermal conductivity and the mass transfer ability, the nickel foam was considered as new prospective catalyst support.[24-26] For instance, Li *et al.* reported the preparation of the nickel foam supported hierarchical monolith Ni@Pd catalysts for benzene hydrogenation which presents high catalytic performance.[25] Xiong *et al.* revealed the excellent catalytic stability as well as the enhanced CO selectivity of Ru_2-ZrO_2/CNT-Ni foam catalysts for the selective CO methanation.[26] They believed that the great catalytic performance was contributed by the high thermal conductivity of nickel foam and the co-effect between the active components and the unique microstructure. However, to the best of our knowledge, the nickel foam has not been studied as a carrier to support the active species for NH_3-SCR of NO.

Inspired by these attractive properties of Ni-Mn bi-metal oxides and the Ni foam support, we fabricated the nickel foam based 3D hierarchical monolith catalysts by the following synthetic route. As demonstrated in the schematic illustration (Fig. 1), the nanosheets are uniformly grown on the bare surface of nickel foam *via* the hydrothermal reaction and the porous structure is formed by the calcination process. During the hydrothermal reaction, the Ni^{2+} ions are firstly dissolved from the Ni foam and then co-precipitated with the Mn^{2+} ions to form Ni-Mn double hydroxides based on the pH-driven dissolution-

Cite this: DOI: 10.1039/c0xx00000x

www.rsc.org/xxxxxx

ARTICLE TYPE

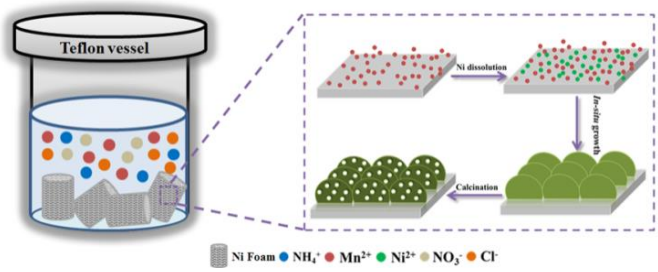

Fig.1 Schematic representation of the synthesis route of 3DH-NM/NF catalysts.

precipitation mechanism.[27] Therefore, the nickel foam not only serves as monolith support, but also provides the Ni^{2+} ions for the *in-situ* fabrication of the Ni-Mn oxide nanosheets in the hydrothermal reaction, which could lead to the strong adhesion between the active species and the support. Afterwards, the calcination procedure could lead to the generation of the Ni-Mn bi-metal oxides. Simultaneously, pores were formed on the Ni-Mn oxides nanosheet structure owing to the gas release during the decomposing of Ni-Mn hydroxide precursors. Additionally, the structures, morphologies, surface properties as well as the catalytic performance of the catalysts are carefully examined. Considering the desirable properties of Mn-Ni oxides and the 3D hierarchical structure, the 3DH-NM/NF catalysts may become an excellent candidate as monolith catalysts for NH_3-SCR.

2. Experimental Section

2.1 Catalysts preparation

All reagents were of analytical grade and used without further purification, supplied by Sinopharm Chemical Reagent Co. Ltd (China). Deionized water was also used in the experiments. Commercial nickel foam was purchased from Alantum Advanced Technology Materials (Dalian, China), Co. Ltd. Before use, the nickel foam was pretreated with 0.1 M HCl aqueous solution upon ultrasonic vibration to remove the grease and the possible surface oxide layer.

In a typical synthesis, 12 mmol of $Mn(NO_3)_2$ and 36 mmol NH_4Cl were dissolved in 80 ml deionized water under stirring for 30 min. Subsequently, 3 cm^3 (640 mg) of the cleaned nickel foams were immersed into the above mentioned homogenous solution and then transferred to a Teflon-lined stainless steel autoclave for 8 h of hydrothermal reaction under 150 ^oC. After the reaction process, the autoclave was allowed to cool down naturally. Then the products were washed by ethanol and deionized water for several times, respectively. Afterwards, the products were dried overnight and finally calcined in air at 500 ^oC for 4 h by a ramping rate of 2 ^oC/min. After that, the desired catalysts were obtained and denoted as 3DH-NM/NF.

For comparison, the NiO nanosheet decorated nickel foam (denoted as 3DH-N/NF) was fabricated *via* the similar route using 12 mmol $Ni(NO_3)_2$ as precursor. The pure nickel foam (denoted as NF) was calcined and examined in order to reveal the differences of the morphology as well as the properties between the decorated surface and the bare surface of NF. Besides, the commercial cordierite supported Ni-Mn oxides (denoted as NM/Cordierite) was also fabricated by a traditional impregnation method (experimental details provided in ESI†).

2.2 Catalysts characterization

The scanning electron microscope (SEM) observation was performed by a JEOL JSM-6700F system, while the Powder X-ray diffraction (XRD) was measured by a Rigaku D/MAX-2200 X-ray diffractometer with Cu-Ka (40 kV, 40 mA) radiation and a secondary beam graphite monochromator. The diffraction data were collected over 2θ range of 10-90 ° with 0.02 ° intervals. The transmission electron microscope (TEM) observation was carried out on a JEOL JEM-200CX system. Energy dispersive X-ray (EDX) analysis and the elemental mapping were conducted using an Inca Energy 200 TEM system from Oxford Instruments. The X-ray photoelectron spectroscopy (XPS) measurements were conducted on a RBD upgraded PHI-5000C ESCA system with a hemispherical energy analyzer using an Mg-Ka (1253.6 eV) anode and a dual X-ray source. Before deconvolution, the binding energies refer to O, Ni and Mn were corrected according to contaminant carbon (C 1s = 284.6 eV) and the peak fitting was performed by using AugerScan (version 3.21) software. Temperature-programmed reduction by hydrogen (H_2-TPR) was carried out on a Tianjin XQ TP5080 auto-adsorption apparatus. Before the reduction process, 40 mg of each catalyst was outgassed at 300 ^oC for 30 min and then cooled down to room temperature. Afterwards, the inlet gas was switched to 10 % H_2/Ar and the reaction temperature was heated to 700 ^oC (heating ramp=10 ^oC min^{-1}) and the H_2 consumption data was recorded by a thermal conductivity detector (TCD). Temperature-programmed desorption experiments of ammonia (NH_3-TPD) were performed on the same apparatus and the desorption amounts of NH_3 was also monitored by the TCD. Prior to TPD, 80 mg of catalysts were outgassed under 300 ^oC for 0.5 h and then cooled to 100 ^oC (under Ar protection). Subsequently, the catalysts were saturated with high-purity anhydrous ammonia at 100 ^oC for 90 min and then the physisorbed ammonium was removed at the same temperature by 1 h Ar flow flushing. Finally, the TPD process was carried out from 100 to 750 ^oC at a ramping rate of 10 ^oC min^{-1} with the protection of Ar flow.

2.3 Catalytic performance tests

The NH_3-SCR activity tests were conducted in a fixed-bed quartz reactor (8 mm of internal diameter) in a steady state flow mode. Before test, 1.5 cm^3 (320 mg) of catalysts and 50 mg quartz wool (to avoid the axial diffusion) were inserted into the reactor. The reactant feed gas composition was list as follow: [NO] = [NH_3] = 500 ppm, [O_2] = 3 vol. %, [H_2O] = 8 vol. % (when used), N_2 as balance gas, and gas hourly space velocity (GHSV) of 20000 h^{-1} was obtained. The SCR reaction was carried out in the

temperature range from 210 to 390 °C and the data was recorded until the reaction reached a steady state. The concentrations of NO in the feed gases and the effluent streams were analyzed continuously by a KM9106 flue gas analyzer, while the concentrations of N_2O and NH_3 were recorded by a Transmitter IR N_2O analyzer and an IQ350 ammonia analyzer. The NO conversion was calculated according to the following expression.

$$\text{NO Conversion}(\%) = \frac{[\text{NO}]_{\text{in}} - [\text{NO}]_{\text{out}}}{[\text{NO}]_{\text{in}}} \times 100\%$$

3. Results and discussion

3.1 Morphology and structure of the catalysts

The morphologies and structures of the catalysts were firstly investigated by the SEM observation. As illustrated in Fig. 2, the nickel foam reveals an interconnected porous framework, which could serve as the support and the growth center of the Ni-Mn oxide nanosheets. Evidently, after the hydrothermal reaction and the calcination process, the nickel substrate is covered by Ni-Mn oxide nanosheets completely (Fig. 2a and Fig.S1, ESI†). The *in-situ* formation of the Ni-Mn oxide nanosheets on the nickel foam substrate could lead to strong adhesion between the nanosheets and the nickel substrate, which could prevent the detachment of active components during the catalysis process. The overall morphologies of these Ni-Mn oxide nanosheets are uniformly arranged and exhibit the 3D structure (Fig. 2b). The thickness of nanosheets is about 30-70 nm and many small holes can be observed on the surface of the nanosheets (Fig. 2c). Similar morphology and porous structure can also be observed on the NiO nanosheets of the 3DH-N/NF catalysts (Fig. S2, ESI†), implicating that the synthetic route could be a common way for *in-situ* fabricating porous metal oxide nanosheets on the nickel foam. The composition and phase structures of Ni-Mn bi-metal oxide nanosheets were determined by the XRD measurement. In order to reduce the impact of the nickel substrate, we scratched the surface of the 3DH-NM/NF catalysts and collected the brown powders for the XRD analysis. As shown in Fig. 2d, the diffraction peaks are related to two crystalline phases: the peaks

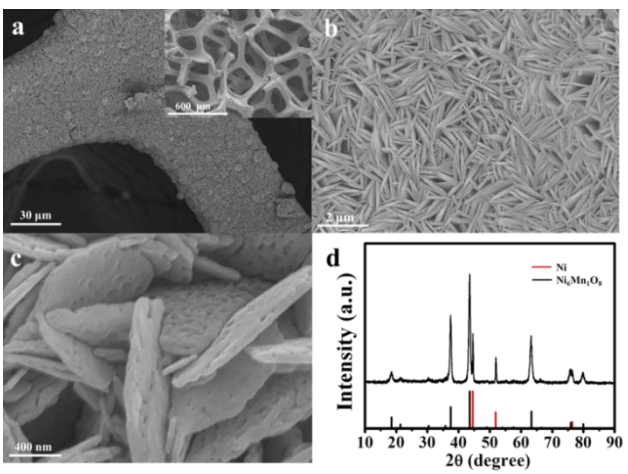

Fig.2 a-c) SEM images of 3DH-NM/NF catalysts d) XRD pattern of 3DH-NM/NF catalysts.

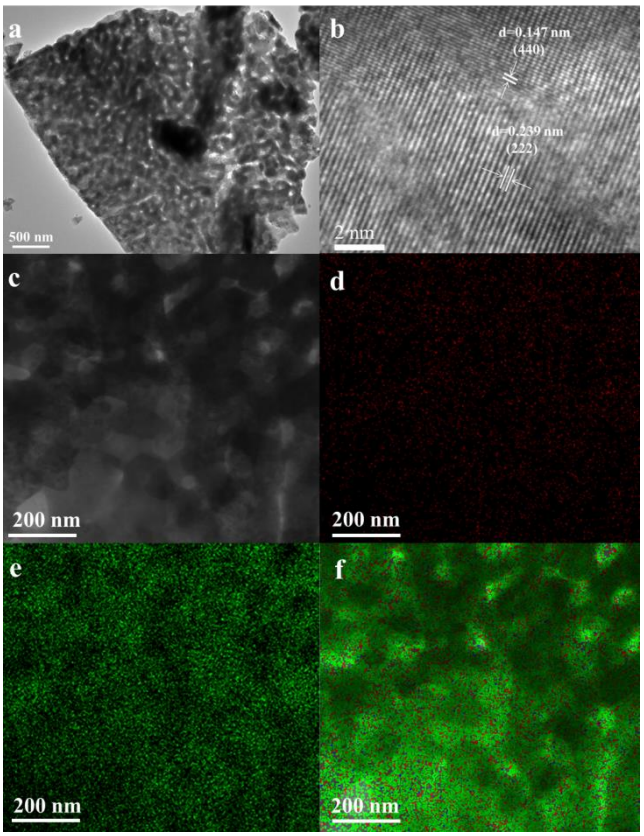

Fig.3 a) TEM image of a single Ni-Mn oxides nanosheet form the 3DH-NM/catalysts, b) HRTEM image of the Ni-Mn oxides nanosheet, c) HAADF-STEM image of the Ni-Mn oxides nanosheet, and d-f) elemental mapping images of Ni-Mn oxides nanosheet.

located at 44.5 °, 51.8 ° and 76.6 ° are assigned to the Ni scratched from the nickel substrate (JCPDS No. 70-0989), while the other peaks are corresponding to the typical $Ni_6Mn_1O_8$ spinel (JCPDS No. 83-1186).[28] These results suggest the formation of Ni-Mn-O solid solution contributed by the uniform distribution of Mn and Ni atoms during the precipitation procedure and the appropriate calcination temperature. Interestingly, the characteristic diffraction peaks related to the manganese oxides or nickel oxides are absent from the XRD pattern, indicating the high purity of the nanosheets obtained from the hydrothermal reaction and the calcination process.

In order to prove further insights of the nanosheets, the TEM observation was employed and the corresponding images are shown in Fig. 3a. As can be seen, some pores are distributed on the nanosheets, which is in good accordance with the SEM observation. The small pores among the nanosheets are formed with the gas release during the decomposing of the metal hydroxide precursors.[29-31] Generally, the 3D hierarchically structures could reduce the mass-transfer resistance and provide more inner surface area for the reaction gas, which is beneficial to the catalytic process.[19, 32] In addition, the high-resolution TEM (HRTEM) image (Fig. 3b) indicates that the inter-planar spacing of distinct fringes are 0.239 nm and 0.147 nm, corresponding to the (222) and (440) planes of the $Ni_6Mn_1O_8$ spinel, which is in good agreement with the XRD pattern. As demonstrated in the

Cite this: DOI: 10.1039/c0xx00000x

www.rsc.org/xxxxxx

ARTICLE TYPE

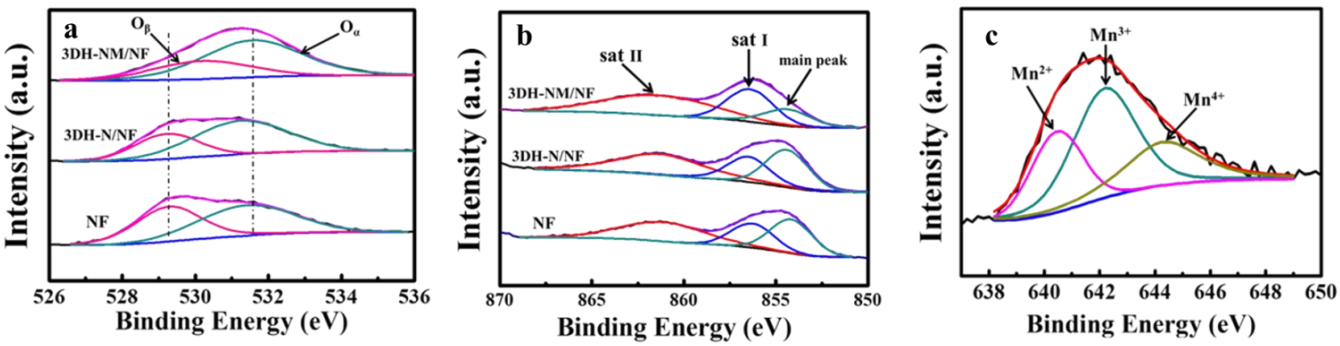

Fig.4 a) O 1s spectra, b) Ni $2p_{3/2}$ spectra of the catalysts, and c) Mn $2p_{3/2}$ of the 3DH-NM/NF catalysts.

Table 1 XPS results of the catalysts

Sample	Surface composition (at.%)			$O_\alpha/(O_\alpha+O_\beta)$ (%)	Sat I/main peak (area ratio)	Sat II/main peak (area ratio)	Mn^{2+} (%)	Mn^{3+} (%)	Mn^{4+} (%)
	Ni	O	Mn						
NF	29.8	70.2	-	53.7	0.72	1.38	-	-	-
3DH-N/NF	31.1	68.9	-	66.1	0.75	1.61	-	-	-
3DH-NM/NF	18.7	78.0	3.3	69.3	1.83	2.71	23.5	47.4	29.1

previous reports[33, 34], the dispersion of active components is crucial to the catalytic activity of catalysts. Therefore, the elemental mapping of the nanosheet from the 3DH-NM/NF catalysts was conducted and the distribution of Ni and Mn atoms are shown in Fig. 3 (d-f). Evidently, the Ni and Mn atoms are uniformly distributed within the porous nanosheet structure, which could lead to strong interaction between the Ni and Mn species.

3.2 XPS analysis

The XPS measurements were performed to study the atom ratios as well as the valence of the near surface components. The mole fractions of O, Ni as well as Mn are listed in Table 1. It is noticeable that 3DH-NM/NF catalysts have higher oxygen concentration (78.0 %) than the 3DH-N/NF (68.9 %) and NF (70.2 %) catalysts, illustrating that more lattice oxygen or surface capping oxygen species are located on the surface of the 3DH-NM/NF catalysts. Moreover, the atomic ratio of Ni versus Mn determined by XPS is 5.67, which is approximate to the theoretical value of $Ni_6Mn_1O_8$ spinel.

Normally, the XPS spectra of O 1s could be fitted into two peaks denoted as O_α and O_β, which are related to two different status of oxygen species.[35] The peak located at 529.6-530.1 eV is ascribed to lattice oxygen and the other centered at 531.3-532.0 eV is the characteristic peak of surface-absorbed oxygen from the oxide defects or hydroxyl groups.[15, 36] As is well known, O_α is more active than the O_β in oxidization reaction. Therefore, higher content of O_α can promote the oxidation of NO to NO_2 at low temperature and thereafter facilitate the "fast SCR" reaction.[6, 37, 38] Thus, the variation of $O_\alpha/(O_\alpha+O_\beta)$ ratio could lead to the diverse performance for NH_3-SCR of NO in the low temperature range. According to the XPS results, the NF catalysts show a $O_\alpha/(O_\alpha+O_\beta)$ ratio of 53.7 %, while the 3DH-N/NF catalysts exhibit a higher $O_\alpha/(O_\alpha+O_\beta)$ ratio of 66.1 %, indicating more oxide defects and hydroxyl groups are formed on the nanosheets than the bare surface of NF, which could be beneficial to the NH_3-SCR of NO. Interestingly, the 3DH-NM/NF catalysts exhibit the highest O_α concentration of 69.3 % and the binding energy of oxygen species moved slightly to higher direction (Fig. 4a), implicating a strong interaction between the oxygen species and the metal species in the bi-metal solid solutions.

Fig. 4b shows the Ni $2p_{3/2}$ spectra of the 3DH-NM/NF, 3DH-N/NF and NF catalysts. For all catalysts, the peaks corresponding to Ni $2p_{3/2}$ are deconvoluted into three peaks located at 861.5 eV, 856.5 eV and 854.4 eV, which are related to the two satellite peak (denoted as Sat I and Sat II) and the main peak of Ni $2p_{3/2}$, respectively. The Sat I peak is corresponding to the Ni^{3+} species, Ni^{2+}-OH species or Ni^{2+} vacancies, while the origin of the Sat II has been ascribed as the characteristic peak of ligand-metal charge transfer.[39-41] Therefore, the area ratio of Sat I/main peak could provide information to the charge imbalance as well as the surface defects of the catalysts and the area ratio of Sat II/main peak could be used to reflect the interaction between the metal species. [40, 41] The area ratio of the Sat I/main peak and the Sat II/main peak are listed in Table 1. It is worth noticing that the 3DH-NM/NF catalysts demonstrated a higher area ratio (1.83) of Sat I/main peak than the 3DH-NM/NF (0.75) and NF (0.72), illustrating more unsaturated Ni atoms and structure defects exist in the Ni-Mn bi-metal oxides. On the other hand, the area ratio of Sat II/main peak of the catalysts can be sequenced as 3DH-NM/NF (2.71) > 3DH-N/NF (1.38) > NF (1.25). Obviously, the area ratio of Sat II/main peak increased significantly after the

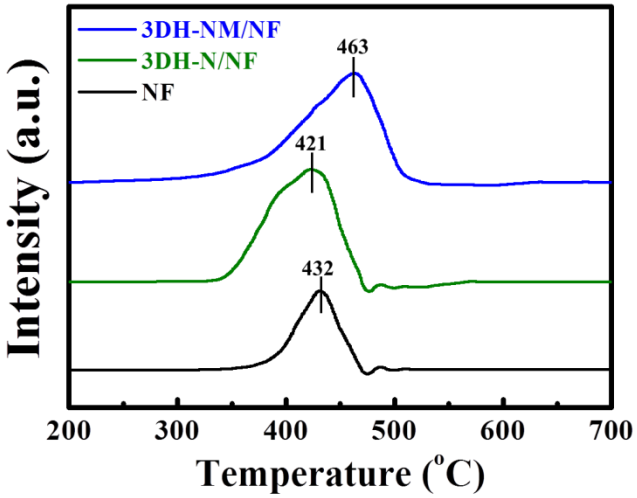

Fig.5 H_2-TPR profiles of the catalysts.

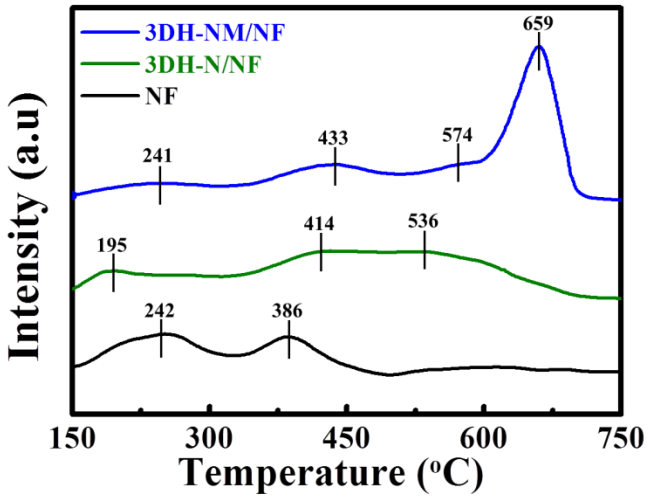

Fig.6 NH_3-TPD profiles of the catalysts.

introduction of Mn species, which could suggest the nature of the surrounding atoms and the structural arrangements on the catalysts surface have been greatly changed by the synergistic effect between the Ni and Mn species.

By deconvolution, the Mn $2p_{3/2}$ spectra of 3DH-NM/NF catalysts can be fitted into three peaks which stand for Mn^{2+} (640.5 eV), Mn^{3+}(642.2 eV) and Mn^{4+}(644.3 eV), respectively.[13] As shown in Table 1 and Fig. 4c, the manganese species is the mixture of Mn^{2+} (23.5 %), Mn^{3+} (47.4 %) and Mn^{4+} (29.1 %), while the Mn^{3+} is the dominant valance state. It is well known that the Mn^{3+} could act as reducible and oxidizable composition in the redox couples of Mn^{3+}/Mn^{2+} and Mn^{3+}/Mn^{4+}.[42] Thus, the high Mn^{3+} ratio could enhance the transforming ability of Mn species between the different valance states, thereafter enrich the redox cycle during the catalytic process.

3.3 H_2-TPR analysis

The H_2-TPR analyses were performed to evaluate the reduction properties of the catalysts. The TPR profiles of the three catalysts are demonstrated in Fig. 5. The NF catalysts show a single reduction peak located at 432 °C, which is corresponding to the reduction of Ni species from Ni^{2+} to Ni.[43] As for the 3DH-N/NF catalysts, the reduction peak shifts slightly to the low temperature range and centered at 421 °C. It suggests that the reduction process is easier to conduct on the Ni-nanosheets than the bare surface of the nickel foam. Moreover, the peak area is increased significantly, convincing more reducible species are exposed on the porous nanosheets. As is well known, the redox properties of catalysts are closely related to the catalytic cycle in the homogeneous catalysis process.[15] Accordingly, the existence of the nanosheet structure could be beneficial to the NH_3-SCR process. Furthermore, for the 3DH-NM/NF catalysts, a broad reduction peak occurred at 463 °C. The peak exhibits obvious difference to the reduction peak of 3DH-N/NF catalysts and the reduction performance is similar to the work by Zhang *et al.* [28] Normally, the reduction of Ni_6MnO_8 can be assumed in two steps as $Ni_6MnO_8 \rightarrow MnO\text{-}NiO + H_2O \rightarrow Ni + MnO$. The MnO_x species are reduced to MnO at the first reduction step, followed by the reduction from NiO to Ni. The XRD pattern has proved that the nanosheet is composed of Ni_6MnO_8 with high purity. Thus, the H_2 consumption peak of 3DH-NM/NF catalysts is the conjunction of the two reduction reactions. Meanwhile, the obvious difference of the reduction peaks between the 3DH-NM/NF and 3DH-N/NF catalysts could reveal the strong interaction between the manganese and the nickel species, which would affect the reducibility as well as the NH_3-SCR catalytic cycle.

3.4 NH_3-TPD analysis

The NH_3-TPD measurements were conducted to study the adsorption behaviour of NH_3 on the catalysts, which is generally considered as one of the primary steps in the NH_3-SCR of NO. [5, 17, 44] As depicted in Fig. 6, the NF catalysts show two distinct desorption peaks located at 242 °C and 386 °C, respectively. Meanwhile, a small peak centered at 195 °C and a board peak composed of two peaks at 414 °C and 536 °C can be observed in the TPD curve of the 3DH-N/NF catalysts. It is generally accepted that the desorption peak at 200-400 °C is corresponding to the weak acid sites, the peak in the temperature range of 400-600 °C is the contribution of medium acid sites and the peak located over 600 °C can be assigned to the strong acid sites.[45-47] Therefore, most of absorbed NH_3 molecules are linked to the weak and medium acid sites on the surface of the NF and 3DH-N/NF catalysts. It is worth noticing that desorption peaks of the 3DH-N/NF catalysts move to higher temperature and become more intense. As is well known, the area and the position of desorption peak is positively related to the amount and strength of the acid sites of the catalysts.[15, 44] Thus, we can draw the conclusion that the *in-situ* formation of nanosheets could lead to the enhancement of the strength and amount for both weak and medium acid sites. Meanwhile, four peaks centered at 241 °C, 433 °C, 474 °C and 659 °C can be observed in the TPD profile of 3DH-NM/NF catalysts. In contrast with the 3DH-N/NF catalysts, the peaks ranging from 200-600 °C were excursed to higher temperature range, indicating the weak and medium acid sites are intensified by the co-effect of the Ni and Mn species. Particularly, a large peak corresponding to the strong acid peaks occurred in the TPD curve of 3DH-NM/NF catalysts, implying the amount of strong acid sites have also been greatly increased by the synergistic effect of Ni and Mn. Catalytically, the enhancement of acid sites could allow more ammonia species to be absorbed

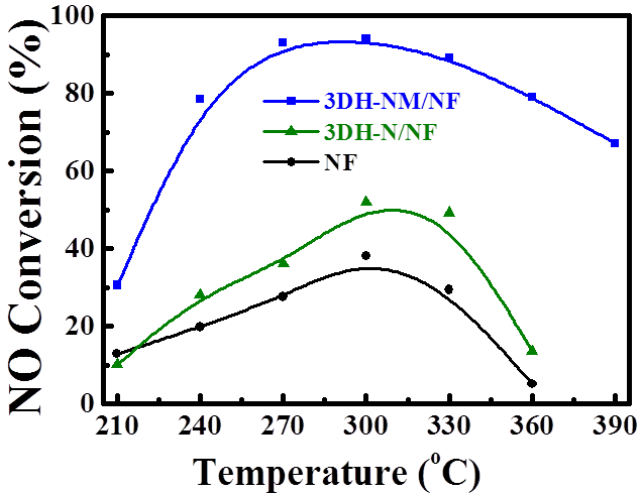

Fig.7 NH_3-SCR performances of catalysts as function of temperatures. Reaction conditions: NO=NH_3= 500 ppm, O_2 = 3 vol. %, N_2 as balance gas, GHSV: 20000 h^{-1}.

on the catalysts surface and then participate in the SCR reaction, which is beneficial to the catalytic activity in the de-NO_x process.[48, 49] Hence, the coating of the porous Ni-Mn bi-metal oxide nanosheets on the nickel foam is advantageous to the NH_3-SCR performance.

3.5 Catalytic performance

As illustrated in Fig. 7, the de-NO_x performance of catalysts was tested as a function of temperature between 210 °C to 420 °C. Obviously, the NF catalysts exhibit limited de-NO_x properties and the maximum NO conversion is only 39 % among the temperature range. It is noted that pure nickel or nickel oxides are not quite active in the NH_3-SCR reaction,[18] which is in good conformity with our experiment. However, when the bare surface of nickel foam is decorated by the porous NiO nanosheets, the catalysts exhibit a better catalytic activity and the maximum NO conversion is increased to 52 %. The enhancement could be related to the higher O_α/ (O_α+ O_β) ratio, enriched surface reducible species as well as the improved weak and medium surface acid sites. Therefore, the formation of porous nanosheet structure on the Ni foam is beneficial to the catalytic activity. Moreover, the 3DH-NM/NF catalysts exhibit a wide temperature window for > 80 % NO conversion ranges from 245 °C to 360 °C and the maximum NO conversion 91 % is achieved at 270 °C. Compared with the NF and 3DH-N/NF catalysts, the 3DH-NM/NF catalysts demonstrated more satisfactory catalytic activity and broader temperature window, illustrating that the special characteristics of 3DH-N/NF catalysts bring about the improved NH_3-SCR performance. The well-ordered nanosheets are composed of $Ni_6Mn_1O_8$ spinel with high purity and the metal species are uniformly dispersed in the bi-metal oxides. Thus, a strong interaction between Ni and Mn species could be observed, which lead to the abundance of the active oxygen species as well as the difference of the redox behavior. As is well known, the strong interaction between the active components could improve the redox catalytic cycle of the corresponding catalysts, resulting in better NH_3-SCR performance of NO.[50-52] On the other hand, the strength and amounts of the surface acid sites have been greatly improved on the catalysts surface, especially for the

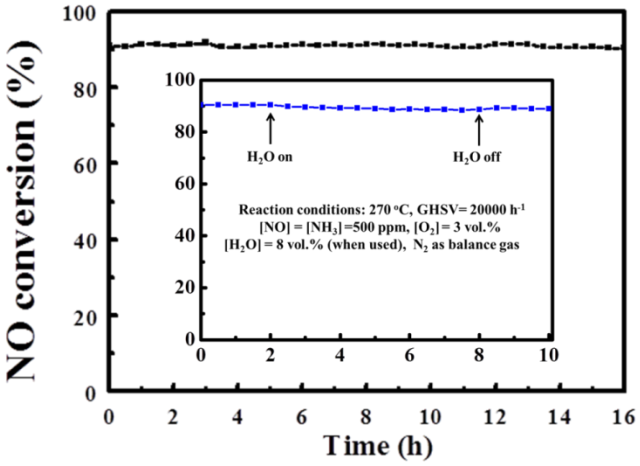

Fig.8 Stability and H_2O tolerance test (inset) of 3DH-NM/NF catalysts.

strong acid sites. That could provide more ammonia absorption and activation sites and then facilitate the NH_3-SCR reaction.[5] Besides, the 3DH-NM/NF catalysts keep a high N_2 selectivity over 90 % until the reaction temperature reached 390 °C (Fig. S3, ESI†), which could explain the high catalytic activity of 3DH-NM/NF between 240 °C to 360 °C. In addition, the 3DH-NM/NF catalysts exhibit relatively higher catalytic activities than the NM/Cordierite catalysts (Fig. S4, ESI†), indicating the advantages of the 3D hierarchical structure and the *in-situ* formation technique. Briefly, the excellent catalytic activity of the 3DH-NM/NF catalysts is mainly contributed by the 3D hierarchical structure, strong synergistic effects between the Mn and Ni species, the enrichment of exposed active sites and structure defects and the enhanced surface acidity.

The stability test was carried out to evaluate the catalytic performance of the 3DH-NM/NF catalysts. As depicted in Fig. 8, the 3DH-NM/NF catalysts were tested under 270 °C. With the elapsed time, the NO conversion rate was maintained at ca. 90 % under the continuous running duration. In order to understand the good performance of the 3DH-NM/NF catalysts in the stability test, the morphology of the used 3DH-NM/NF catalysts was carefully examined by SEM observation. As shown in Fig. 9, the morphologies and structures of the catalysts are well-maintained after the stability test. Thus, it can be concluded that the adhesion between the Ni-Mn oxide nanosheets and the nickel foam is sufficiently strong to support the de-NO_x process. Moreover, the Ni foam supports could offer high thermal conductivity during the catalytic procedure,[26] which leads to the inhibition of sintering on the catalysts surface. Furthermore, it has been demonstrated that the Mn-containing spinel structure is relatively

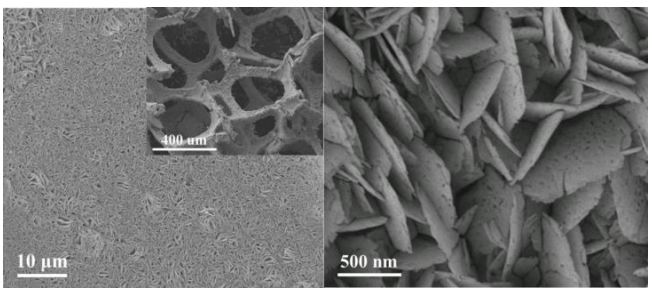

Fig.9 SEM images of 3DH-NM/NF catalysts after the stability test.

stable in many catalytic reactions.[11, 33, 53] As a result, the aggregation of the well dispersed Ni and Mn species should be restrained in the spinel phase. Generally, it is reasonable to deduce that the good catalytic cycle stability of the 3DH-NM/NF catalysts is contributed by these attractive features.

Normally, the H_2O had an inhibition effect on the NH_3-SCR of NO.[54-56] Thus, the H_2O-resistant test was conducted and the test result was demonstrated in the insert of Fig. 8. With the H_2O (8 vol. %) in the inlet gas, only a slight decrease (about 2 %) of NO conversion can be observed in the 6 h reaction time. While H_2O was turned off, the catalytic activity of 3DH-NM/NF catalysts restored to the initial state. Accordingly, the 3DH-NM/NF catalysts exhibit excellent H_2O resistance performance. It has been demonstrated that competitive adsorption between H_2O and NH_3 molecules on the active sites is the main reason for the decrease of catalytic activity in the H_2O containing gas flow.[13, 56, 57]Consequently, the high anti-H_2O ability of 3DH-NM/NF catalysts is mainly due to the preferential absorption of NH_3 on the catalysts surface, which is contributed by the abundant acid sites of 3DH-NM/NF. In addition, the 3DH-NM/NF catalysts maintained the high catalytic activity with the altering of the space velocity (Fig. S5, ESI†). According to these favourable properties, the 3DH-NM/NF catalysts could be considered as a promising candidate for the monolith de-NO_x catalysts.

4. Conclusions

In summary, we successfully prepared the nickel foam based 3D hierarchical monolith catalysts *via* a simple hydrothermal reaction and calcination process. These catalysts exhibited excellent NH_3-SCR activity of NO and good water resistance. The favourable properties arise from the 3D hierarchical structure, the enriched active oxygen species and reducible species, the enhanced surface acidity as well as the synergetic effects between the well dispersed Mn and Ni species. In addition, the *in-situ* formation of the porous Ni-Mn oxide nanosheets on the Ni foam brought about the strong adhesion between the active components and catalysts support, which lead to the expected stability during the catalytic process. Therefore, this eco-friendly and easily constructed 3D hierarchical catalysts with good catalytic performance could open up great opportunities for applications of monolith de-NO_x catalysts.

Acknowledgements

The authors acknowledge the support of the National Natural Science Foundation of China (51108258), the Shanghai Municipal Education Commission (14ZZ097), the Science and Technology Commission of Shanghai Municipality (11NM0502200, 13NM1401200 &11NM0502300) and Dongguan Municipal Research Program for Colleges and Institutes (201210825000535).

Notes and references

Research Center of Nano Science and Technology, School of Material Science and Engineering, Shanghai University, Shanghai 200444, China. Fax: +86-21-66136079; Tel: +86-21-66136081; E-mail: dszhang@shu.edu.cn

† Electronic Supplementary Information (ESI) available: expermental details and catalytic performance of the NM/Cordierite catalysts, SEM image and EDX analysis of the NF and 3DH-N/NF catalysts, N_2 selectivity and catalytic performance under different gas hourly space velocity of the 3DH-NM/NF catalysts. See DOI: 10.1039/b000000x/

1. S. Beirle, K. F. Boersma, U. Platt, M. G. Lawrence and T. Wagner, *Science*, 2011, **333**, 1737-1739.
2. C. H. Kim, G. Qi, K. Dahlberg and W. Li, *Science*, 2010, **327**, 1624-1627.
3. C. Johnson, J. Henshaw and G. Mclnnes, *Nature*, 1992, **355**, 69-71.
4. J. D. Felix, E. M. Elliott and S. L. Shaw, *Environ. Sci. Technol.*, 2012, **46**, 3528-3535.
5. X. Mou, B. Zhang, Y. Li, L. Yao, X. Wei, D. S. Su and W. Shen, *Angew.Chem.*, 2012, **51**, 2989-2993.
6. W. Wang, G. McCool, N. Kapur, G. Yuan, B. Shan, M. Nguyen, U. M. Graham, B. H. Davis, G. Jacobs, K. Cho and X. Hao, *Science*, 2012, **337**, 832-835.
7. P. Forzatti, I. Nova and E. Tronconi, *Angew.Chem.*, 2009, **48**, 8366-8368.
8. P. G. W. A. Kompio, A. Brückner, F. Hipler, G. Auer, E. Löffler and W. Grünert, *J. Catal.*, 2012, **286**, 237-247.
9. X. Wang, A. Shi, Y. Duan, J. Wang and M. Shen, *Catal. Sci. Technol.*, 2012, **2**, 1386.
10. E. Garciabordeje, *J. Catal.*, 2004, **223**, 395-403.
11. S. Yang, C. Wang, J. Li, N. Yan, L. Ma and H. Chang, *Appl. Catal., B*, 2011, **110**, 71-80.
12. Thirupathi, Boningari, Smirniotis and P. G., *J. Catal.*, 2012, **288**, 74-83.
13. C. Fang, D. Zhang, S. Cai, L. Zhang, L. Huang, H. Li, P. Maitarad, L. Shi, R. Gao and J. Zhang, *Nanoscale*, 2013, **5**, 9199-9207.
14. J. Yang, H. Ma, Y. Yamamoto, J. Yu, G. Xu, Z. Zhang and Y. Suzuki, *Chem. Eng. J.*, 2013, **230**, 513-521.
15. L. Zhang, D. Zhang, J. Zhang, S. Cai, C. Fang, L. Huang, H. Li, R. Gao and L. Shi, *Nanoscale*, 2013, **5**, 9821-9829.
16. S. Yang, Y. Fu, Y. Liao, S. Xiong, Z. Qu, N. Yan and J. Li, *Catal. Sci. Technol.*, 2014, **4**, 224-232.
17. R. Zhang, W. Yang, N. Luo, P. Li, Z. Lei and B. Chen, *Appl. Catal., B*, 2014, **146**, 94-104.
18. Y. Wan, W. Zhao, Y. Tang, L. Li, H. Wang, Y. Cui, J. Gu, Y. Li and J. Shi, *Appl. Catal., B*, 2014, **148-149**, 114-122.
19. L. L. Li, J. Xu, Q. Yuan, Z. X. Li, W. G. Song and C. H. Yan, *Small*, 2009, **5**, 2730-2737.
20. B. Pereda-Ayo, U. De La Torre, M. Romero-Sáez, A. Aranzabal, J. A. González-Marcos and J. R. González-Velasco, *Catal. Today*, 2013, **216**, 82-89.
21. M. Valencia, E. López, S. Andrade, M. L. Iris, V. R. Pérez, C. Salinas Martínez de Lecea and A. Bueno López, *Catal. Commun.*, 2014, **46**, 86-89.
22. S. Suarez, J. Martin, M. Yates, P. Avila and J. Blanco, *J. Catal.*, 2005, **229**, 227-236.
23. H. Li, D. Zhang, P. Maitarad, L. Shi, R. Gao, J. Zhang and W. Cao, *Chem.Commun.*, 2012, **48**, 10645-10647.
24. C. Yuan, H. B. Wu, Y. Xie and X. W. Lou, *Angew.Chem.*, 2014, DOI: 10.1002/anie.201303971.
25. Y. Li, L. Zhu, K. Yan, J. Zheng, B. H. Chen and W. Wang, *Chem. Eng. J.*, 2013, **226**, 166-170.
26. J. Xiong, X. Dong, Y. Song and Y. Dong, *J. Power Sources*, 2013, **242**, 132-136.
27. J. Tian, Z. Xing, Q. Chu, Q. Liu, A. M. Asiri, A. H. Qusti, A. O. Al-Youbi and X. Sun, *CrystEngComm*, 2013, **15**, 8300-8305.
28. Y. Zhang, Z. Qin, G. Wang, H. Zhu, M. Dong, S. Li, Z. Wu, Z. Li, Z. Wu, J. Zhang, T. Hu, W. Fan and J. Wang, *Appl. Catal., B*, 2013, **129**, 172-181.
29. H. B. Wu, H. Pang and X. W. Lou, *Energ Environ. Sci.*, 2013, **6**, 3619-3626.
30. G. Zhao, Z. Xu and K. Sun, *J. Mater. Chem. A*, 2013, **1**, 12862-12867.
31. L. Yu, L. Zhang, H. B. Wu, G. Zhang and X. W. Lou, *Energ Environ. Sci.*, 2013, **6**, 2664-2671.
32. L.-H. Chen , X.-Y. Li, G. Tian, Y. Li, J. C. Rooke, G.-S. Zhu, S.-L. Qiu, X.-Y. Yang and B.-L. Su, *Angew.Chem.*, 2011, **50**, 11156-11161.

33. D. Wang, X. Chen, D. G. Evans and W. Yang, *Nanoscale*, 2013, **5**, 5312-5315.
34. A. H. Lu, W. C. Li, Z. Hou and F. Schuth, *Chem.Commun.*, 2007, 1038-1040.
35. S. Cai, D. Zhang, L. Zhang, L. Huang, H. Li, R. Gao, L. Shi and J. Zhang, *Catal. Sci. Technol.*, 2014, **4**, 93-101.
36. Y. Shu, H. Sun, X. Quan and S. Chen, *J. Phys. Chem. C*, 2012, **116**, 25319-25327.
37. F. L. a. H. He, *J. Phys. Chem. C*, 2010, 16929-16936.
38. W. Shan, F. Liu, H. He, X. Shi and C. Zhang, *Chem.Commun.*, 2011, **47**, 8046-8048.
39. B. Solsona, P. Concepción, B. Demicol, S. Hernández, J. J. Delgado, J. J. Calvino and J. M. López Nieto, *J. Catal.*, 2012, **295**, 104-114.
40. B. Solsona, J. M. López Nieto, P. Concepción, A. Dejoz, F. Ivars and M. I. Vázquez, *J. Catal.*, 2011, **280**, 28-39.
41. X.-K. K. Bin Zhao, Jian-Hua Bao, Chun-Ling Wang, Lin Dong, Yu-Wen Chen, and a. H.-L. Chen, *J. Phys. Chem. C*, 2009, 14440-14447.
42. H. Pérez, P. Navarro, J. J. Delgado and M. Montes, *Appl. Catal., A*, 2011, **400**, 238-248.
43. J. C. H. Jose´ A. Rodriguez, Anatoly I. Frenkel,Jae Y. Kim, and Manuel Pe´rez, *J. Am. Chem. Soc.*, 2002, **124**, 346-354.
44. G. Marban, *J. Catal.*, 2004, **226**, 138-155.
45. Y. Shen and S. Zhu, *Catal. Sci. Technol.*, 2012, **2**, 1806-1810.
46. D. Zhang, L. Zhang, L. Shi, C. Fang, H. Li, R. Gao, L. Huang and J. Zhang, *Nanoscale*, 2013, **5**, 1127-1136.
47. Z. Wu, R. Jin, Y. Liu and H. Wang, *Catal. Commun.*, 2008, **9**, 2217-2220.
48. Y. Peng, R. Qu, X. Zhang and J. Li, *Chem.Commun.*, 2013, **49**, 6215-6217.
49. D. Wang, L. Zhang, K. Kamasamudram and W. S. Epling, *ACS Catalysis*, 2013, **3**, 871-881.
50. R. Gao, D. Zhang, X. Liu, L. Shi, P. Maitarad, H. Li, J. Zhang and W. Cao, *Catal. Sci. Technol.*, 2013, **3**, 191-199.
51. Z. Chen, Q. Yang, H. Li, X. Li, L. Wang and S. Chi Tsang, *J. Catal.*, 2010, **276**, 56-65.
52. P. Maitarad, D. Zhang, R. Gao, L. Shi, H. Li, L. Huang, T. Rungrotmongkol and J. Zhang, *J. Phys. Chem. C*, 2013, **117**, 9999-10006.
53. T. Tabakova, V. Idakiev, G. Avgouropoulos, J. Papavasiliou, M. Manzoli, F. Boccuzzi and T. Ioannides, *Appl. Catal., A*, 2013, **451**, 184-191.
54. F. Liu, H. He, Z. Lian, W. Shan, L. Xie, K. Asakura, W. Yang and H. Deng, *J. Catal.*, 2013, **307**, 340-351.
55. Z. Huang, Z. Liu, X. Zhang and Q. Liu, *Appl. Catal., B*, 2006, **63**, 260-265.
56. P. Hu, Z. Huang, W. Hua, X. Gu and X. Tang, *Appl. Catal., A*, 2012, **437-438**, 139-148.
57. F. Liu and H. He, *Catal. Today*, 2010, **153**, 70-76.